J/M PAPERS

Ion emission from nanodroplets undergoing Coulomb explosions: a continuum numerical study

Kaartikey Misra[1] **and Manuel Gamero-Castaño**[1],†

[1]Department of Mechanical and Aerospace Engineering, University of California, Irvine, CA 92697, USA

A droplet charged above the Rayleigh limit is unstable. In the resulting dynamical process, referred to as a Coulomb explosion, smaller droplets with higher charge-to-mass ratios are ejected, reducing the charge of the parent droplet below the Rayleigh limit. Furthermore, if the droplet is sufficiently small, the electric field on its surface can promote ion field emission. Ion emission can lower the charge of a spherical droplet below its Rayleigh limit, keeping it stable, or reduce the charge of a deforming droplet, changing its dynamics and potentially preventing the Coulomb explosion. This article develops a continuum phase field electrohydrodynamic model to study the interplay between Coulomb explosions and ion emission, using charged nanodroplets of the ionic liquid 1-ethyl-3-methylimidazolium bis(trifluoromethylsulfonyl)imide (EMI-Im) as a case study. In small droplets (diameter $D \lesssim 20$ nm for EMI-Im), the electric field is strong enough to emit ions in the early phase of the droplet's evolution, suppressing the Coulomb explosion. For $20 \lesssim D \lesssim 45$ nm, the electric field on the EMI-Im droplet may not promote significant ion emission; however, as the unstable droplet becomes ellipsoidal, ions are emitted from its vertices, ultimately suppressing the Coulomb explosion while shedding 20–40 % of the initial charge. For larger EMI-Im droplets, $45 \lesssim D \lesssim 100$ nm, the evolution typical of a Coulomb explosion is observed, accompanied by ion emission which is however insufficient to prevent the Coulomb explosion. Ion emission and the smaller progeny droplets account for 24 % and 16 % of the initial charge, respectively.

Key words: breakup/coalescence, electrohydrodynamic effects

† Email address for correspondence: mgameroc@uci.edu

K. Misra and M. Gamero-Castaño

1. Introduction

Electrosprays operating in the cone-jet mode (Zeleny 1917; Taylor 1964; Cloupeau & Prunet-Foch 1989; Fernández De La Mora & Loscertales 1994; Collins *et al.* 2008) have the unique ability for producing sprays of charged droplets with narrow size distributions, down to radii of a few nanometres (De Juan & Fernández De La Mora 1997; Rosell-Llompart, Grifoll & Loscertales 2018). The fate of these droplets is governed by the amount of charge they carry relative to their size which, when sufficiently high, can lead to the disintegration of the droplet and/or the shedding of charge by ion field emission. Rayleigh (1882) predicted that a spherical droplet charged beyond a critical value, referred to as the Rayleigh limit, is unstable and will disintegrate. This process is called the Rayleigh fission or Coulomb explosion of the droplet. The pressures inside and outside of the droplet are equal at the Rayleigh limit, i.e. the mechanical and electrical contributions to the surface tension cancel out one another (Rayleigh 1882; Taylor 1964; Basaran & Scriven 1989). This condition can be written in terms of the charge Q_{Ray} carried by the droplet or the strength of the electric field E_{Ray} on its surface:

$$Q_{Ray} = 8\pi\sqrt{\varepsilon_o \gamma R^3}, \quad E_{Ray} = \sqrt{\frac{4\gamma}{\varepsilon_o R}}, \quad (1.1a,b)$$

where γ and R are the surface tension and the radius of the droplet, respectively, and ε_o is the permittivity of vacuum. A droplet charged at or above the Rayleigh limit will undergo a Coulomb explosion, shedding a fraction of its charge and mass in the form of smaller progeny droplets. Interested readers may refer to the photographs of Coulomb explosions taken by Gomez & Tang (1994), Duft *et al.* (2003) and Giglio *et al.* (2008).

The prediction of Rayleigh motivated several experimental studies. Doyle, Moffett & Vonnegut (1964) used Millikan's oil drop technique to study the Coulomb explosion of evaporating aniline and water droplets. They estimated a charge loss of roughly 30 % in the form of smaller progeny droplets, with very low mass loss. Schweizer & Hanson (1971) reported a charge and mass loss of 25 % and 5 %, respectively. Duft *et al.* (2003) used an electrohydrodynamic levitation technique coupled with high-resolution time-elapse photography to isolate a charged droplet and capture the transient behaviour of the Coulomb explosion; they reported a charge loss of 33 % and a mass loss smaller than 1 %. Giglio *et al.* (2008) conducted similar experiments and also performed numerical simulations. They also reported an experimental charge loss of 33 %. Other studies report charge losses between 20 %–40 % (Roulleau & Desbois 1972; Taflin, Ward & Davis 1989), with the exception of sulphuric acid droplets which lose 50 % of their original charge (Richardson, Pigg & Hightower 1989). The images captured by Duft *et al.* (2003) and Giglio *et al.* (2008) have encouraged analytical and numerical computations of the transient behaviour of exploding droplets under different Reynolds numbers (Betelú *et al.* 2006; Burton & Taborek 2011; Collins *et al.* 2013; Radcliffe 2013; Garzon, Gray & Sethian 2014; Gawande, Mayya & Thaokar 2017, 2020). The experimental and numerical evidence show that a Coulomb explosion can be described as a three-step process: first, the slightly perturbed spherical droplet elongates into an ellipsoid of increasing aspect ratio, which eventually develops conical tips at the vertices; second, a fine jet is issued from each cusp and accelerated by the axial electric field; third, the jets, which are naturally unstable, break into progeny droplets which may undergo further Coulomb explosions depending on their electrification level.

Ion field emission is a second mechanism by which a droplet can shed charge. It is a kinetic process in which ions evaporating from the surface of a liquid must overcome an energy barrier (the ion solvation energy), which is lowered by the electric field. Early experiments demonstrated that ion field emission occurs in charged nanodroplets (Iribarne & Thomson 1976; Thomson & Iribarne 1979; Katta, Rockwood & Vestal 1991). Loscertales & Fernández De La Mora (1995) analysed the solid residues left behind by charged nanodroplets after complete evaporation of the liquid phase to quantify the electric field required for ion field emission. Labowsky, Fenn & Fernández De La Mora (2000) developed a continuum ion evaporation model that was in good agreement with the experimental findings of Gamero-Castaño & Fernández De La Mora (2000*b*) and Hogan & Fernández De La Mora (2009). These studies predict the electric field E^* necessary for ion emission to be in the range 0.8–$2 \, \mathrm{V \, nm^{-1}}$, which is only possible in highly charged droplets with diameters of tens of nanometres or smaller. These droplets can originate from much larger droplets in aerosols, where large residence times combined with solvent evaporation lead to a chain of Coulomb explosions producing increasingly smaller droplets. Alternatively, highly charged nanodroplets can be directly produced by electrospraying liquids with high electrical conductivities (Gamero-Castaño & Cisquella-Serra 2020; Miller *et al.* 2021; Perez-Lorenzo & Fernández De La Mora 2022).

The nanodroplets produced by electrospraying highly conducting liquids are often charged above the Rayleigh limit (Gamero-Castaño & Cisquella-Serra 2020; Miller *et al.* 2021; Perez-Lorenzo & Fernández De La Mora 2022). Moreover, Gamero-Castaño & Cisquella-Serra (2020) and Perez-Lorenzo & Fernández De La Mora (2022) observe that a significant fraction of the total current in these electrosprays is carried by ions, e.g. 20–25 % of the total current in electrosprays of EMI-Im and 1-ethyl-3-methylimidazolium tris(perfluoroethyl)trifluorophosphate (EMI-FAP). Both studies find that the ions must be evaporating from droplets in flight and propose that, in some cases, the emission occurs from droplets undergoing Coulomb explosions. The general consensus is that ions will evaporate from the surface of the droplet if the field emission limit is reached before the Rayleigh limit, i.e. if $E_{Ray} > E^*$ (Iribarne & Thomson 1976; Labowsky 1998; Labowsky *et al.* 2000). However, a droplet charged above the Rayleigh limit and having an electric field smaller than E^* may develop areas with larger electric fields during the Coulomb explosion and emit ions. This shedding of charge may reduce substantially the net charge of the parent droplet, modify the dynamics of the Coulomb explosion and even prevent it.

The goal of this article is to study the interaction between a Coulomb explosion and ion field emission in highly charged nanodroplets. We develop an electrohydrodynamic, phase field model to compute the deformation of a droplet charged above the Rayleigh limit, while including ion field emission. We use this model to study EMI-Im nanodroplets in the diameter range 10–100 nm, because experiments show the simultaneous presence of Coulomb explosions and ion field emission under these conditions (Gamero-Castaño & Cisquella-Serra 2020). We address two specific questions: the extent to which ion emission suppresses Coulomb explosions and the magnitude of the charge emitted from typical nanodroplets. The remainder of this article is organized as follows: § 2 describes the numerical model; § 3.1 analyses the Coulomb explosion in the absence of ion emission, with the goals of setting a baseline and validating the numerical model; § 3.2 analyses the effects of ion emission in droplets of varying size charged above the Rayleigh limit; and § 4 summarizes the findings and recommends future work.
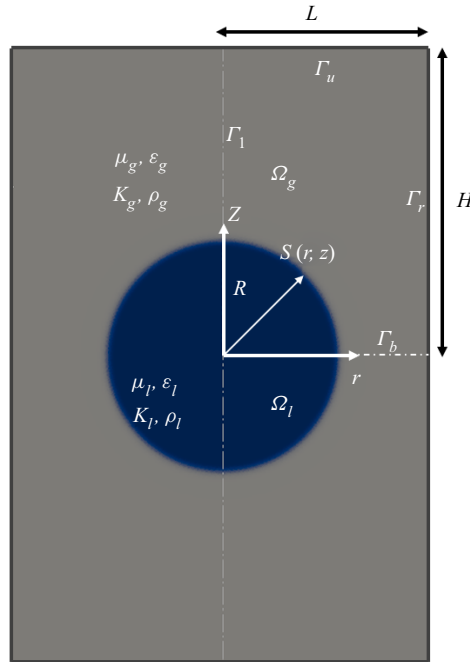
Figure 1. Schematic of the problem and computational domain.

2. Problem formulation and numerical set-up

2.1. *Problem formulation*

Figure 1 shows the computational domain in cylindrical coordinates $\{r, z\}$. There are two subdomains, Ω_l and Ω_g, occupied by an ionic liquid and ambient gas, respectively. The ionic liquid forms a spherical droplet of radius R centred in the origin of coordinates, with a net charge exceeding the Rayleigh limit, $Q_o = \eta Q_{Ray}$ with $\eta > 1$. The droplet is slightly deformed to make it spheroidal while keeping its volume, such that the major axis (along z) is 1.04 times the minor axis (Burton & Taborek 2011; Giglio *et al.* 2020). The droplet is then allowed to evolve from this starting configuration. The problem exhibits axial and planar ($z = 0$) symmetries, and therefore the governing equations are solved in the quadrant bounded by segments Γ_b, Γ_r, Γ_u and Γ_l. The viscosity, density, relative permittivity and electrical conductivity of the media are μ_i, ρ_i, ε_i and K_i, respectively, where the subscript i denotes the ambient gas (g) or the ionic liquid (l).

Electrohydrodynamic problems involving a free surface are usually solved using the leaky dielectric model (Melcher & Taylor 1969; Saville 1997), which treats the interface between the liquid and the surrounding gas as a surface. All excess charge is assumed to reside on the surface (surface charge). Conservation of charge is fulfilled by imposing a conservation equation on the surface, together with an Ohms law and the assumption of negligible volumetric charge in the bulk of the liquid. Drawbacks include the difficult calculation of the position of the free surface and the failure of model assumptions in ultra-fast liquid disintegration (Ganán-Calvo *et al.* 2016; Pillai *et al.* 2016). To avoid these problems, we use the phase field method (Anderson, Mcfadden & Wheeler 1998; Jacqmin 1999; Yue *et al.* 2004). This method regards the interface as a thin region of finite thickness, which can be easily tracked, and a continuous distribution of all independent variables throughout the media. It has the additional advantage of eliminating

the assumption of negligible volumetric charge in the bulk of the liquid. The phase field method has been proven to be accurate in a variety of electrohydrodynamic problems (Tomar *et al.* 2007; López-Herrera, Popinet & Herrada 2011; López-Herrera *et al.* 2015; Mandal *et al.* 2015; Ganán-Calvo *et al.* 2016; Pillai *et al.* 2016).

We have previously developed an electrohydrodynamic phase field model for electrified jets and validated it with existing experimental and numerical results (Misra & Gamero-Castaño 2022). The ionic liquid and the surrounding gas are modelled as a continuum by defining a scalar phase variable ϕ that varies uniformly across the two media. Here, ϕ is tracked using the Cahn–Hilliard equations (Anderson *et al.* 1998), which is assigned values of -1 and 1 in the gas and the liquid far from the interface, respectively. The surface separating the gas and liquid phases is defined as the loci where $\phi = 0$. The physical properties are defined as continuous functions of ϕ throughout the media. Specifically, ρ, μ and ε are the weighted arithmetic means of the phase variable:

$$\rho = \rho_g \left(\frac{1-\phi}{2} \right) + \rho_l \left(\frac{1+\phi}{2} \right), \quad \mu = \mu_g \left(\frac{1-\phi}{2} \right) + \mu_l \left(\frac{1+\phi}{2} \right),$$

$$\varepsilon = \varepsilon_g \left(\frac{1-\phi}{2} \right) + \varepsilon_l \left(\frac{1+\phi}{2} \right), \tag{2.1a–c}$$

whereas, to mitigate unphysical charge leakage, the electrical conductivity is defined as

$$\frac{1}{K} = \frac{1}{K_g} \left(\frac{1-\phi}{2} \right) + \frac{1}{K_l} \left(\frac{1+\phi}{2} \right) \tag{2.2}$$

(Tomar *et al.* 2007; López-Herrera *et al.* 2011; Roghair *et al.* 2015; Huh & Wirz 2022). Presently, the model of Misra & Gamero-Castaño (2022) is supplemented with the standard transport equation for ion field emission (Iribarne & Thomson 1976; Loscertales & Fernández De La Mora 1995):

$$J_i = \frac{k_B T}{h} \sigma \exp \left(-\frac{\Delta G - G(E_n^g)}{k_B T} \right), \tag{2.3}$$

where J_i is the ion current density evaporated from the surface, k_B is the Boltzmann constant, T is the temperature of the liquid, σ is the surface charge density and h is Planck's constant. Here, $\Delta G - G(E_n^g)$ is the energy barrier that the evaporating ion must overcome. Additionally, ΔG is the ion solvation energy, which is not accurately known for ionic liquids although it is estimated to be in the range of 1.4–2 eV (Iribarne & Thomson 1976; Loscertales & Fernández De La Mora 1995; Gamero-Castaño & Fernández De La Mora 2000*a*,*c*). Also, $G(E_n^g)$ is the reduction of the energy barrier due to the normal component of the electric field on the gas side of the surface E_n^g. We use the model by Iribarne & Thomson (1976) to evaluate the reduction of the energy barrier:

$$G(E_n^g) = \left(\frac{e^3 E_n^g}{4\pi\varepsilon_o} \right)^{1/2}, \tag{2.4}$$

where e stands for the elementary unit charge. Equation (2.3) suggests that a meaningful ion current can only occur when $\Delta G - G(E_n^g) = O(k_B T)$. Since $k_B T \ll \Delta G$ at room conditions, the characteristic electric field for ion field emission is given by

(Coffman *et al.* 2016; Coffman, Martínez-Sánchez & Lozano 2019; Gallud & Lozano 2022):

$$E^* = \frac{4\pi\varepsilon_o \Delta G^2}{e^3}. \tag{2.5}$$

The dependent variables velocity $\boldsymbol{u}$, pressure p, volumetric charge density ρ_e, electric potential V and the phase variable ϕ fulfil the equations of conservation of mass, momentum and charge, a modified Poisson's equation and the Cahn–Hillard equation throughout the computational domain:

$$\boldsymbol{\nabla} \cdot \boldsymbol{u} = 0, \tag{2.6}$$

$$\frac{\partial(\rho\boldsymbol{u})}{\partial t} + \boldsymbol{\nabla} \cdot (\rho\boldsymbol{u}\boldsymbol{u}) = -\boldsymbol{\nabla}p + \boldsymbol{\nabla} \cdot (\mu(\boldsymbol{\nabla}\boldsymbol{u} + \boldsymbol{\nabla}\boldsymbol{u}^{\mathrm{T}})) + \boldsymbol{F}_{es} + \boldsymbol{F}_{st}, \tag{2.7}$$

$$\frac{\partial\rho_e}{\partial t} + \boldsymbol{\nabla} \cdot (\rho_e\boldsymbol{u}) = -\boldsymbol{\nabla} \cdot (K\boldsymbol{E}) - \frac{k_B T}{h}\rho_e \exp\left(-\frac{\Delta G - G(E_n^g)}{k_B T}\right), \tag{2.8}$$

$$\varepsilon\nabla^2 V + \boldsymbol{\nabla}V \cdot \boldsymbol{\nabla}\varepsilon = -\frac{\rho_e}{\varepsilon_o}, \tag{2.9}$$

$$\frac{\partial\phi}{\partial t} + \boldsymbol{u} \cdot \boldsymbol{\nabla}\phi = \zeta\gamma\nabla^2\psi, \quad \psi = \frac{1}{\xi}(\phi^2 - 1)\phi - \xi\nabla^2\phi. \tag{2.10a,b}$$

Here, $\boldsymbol{F}_{es}$ and $\boldsymbol{F}_{st}$ are the electrostatic and surface tension volumetric forces:

$$\boldsymbol{F}_{es} = \boldsymbol{\nabla} \cdot \boldsymbol{T}_e = \boldsymbol{\nabla} \cdot \varepsilon\varepsilon_o\left(\boldsymbol{EE} - \frac{1}{2}\boldsymbol{I}|\boldsymbol{E}|^2\right) = \rho_e\boldsymbol{E} - \frac{1}{2}\varepsilon_o\boldsymbol{E} \cdot \boldsymbol{E}\boldsymbol{\nabla}\varepsilon, \tag{2.11}$$

$$\boldsymbol{F}_{st} = \gamma\psi\boldsymbol{\nabla}\phi. \tag{2.12}$$

The volumetric charge conservation equation (2.8) can be derived from the general Poisson–Nernst–Planck (PNP) equation for charged species (Saville 1997; Herrada *et al.* 2012; Gañán-Calvo *et al.* 2018), see Appendix B for further details. The equation includes charge convection and conduction, and a term accounting for the loss of charge due to ion field emission. Equation (2.10a,b) is the Cahn–Hillard equation for the phase variable ϕ (Anderson *et al.* 1998; Jacqmin 1999, 2000; Yue *et al.* 2004); ζ is the phase field mobility parameter (a constant) and ξ is the diffuse interface thickness which is indicative of the sharpness of the artificial interface separating the two phases. Brackbill, Kothe & Zemach (1992), Jacqmin (2000), Anderson *et al.* (1998), Jacqmin (1999) and Yue *et al.* (2004) provide derivations of the surface tension force, (2.12). It is worth noting that in the sharp interface limit, $\xi \to 0$, the phase field formulation transforms into the conventional treatment based on the use of a surface (Brackbill *et al.* 1992; Yue *et al.* 2004). We employ the following boundary conditions:

$$\boldsymbol{e}_z \cdot \boldsymbol{E} = 0, \quad \boldsymbol{e}_z \cdot \boldsymbol{u} = 0, \quad \boldsymbol{e}_z \cdot \boldsymbol{\nabla}\psi = \boldsymbol{e}_z \cdot \boldsymbol{\nabla}\phi = 0, \quad \text{on } \Gamma_b, \tag{2.13}$$

$$V = 0, \quad \boldsymbol{u} = 0, \quad \boldsymbol{e}_r \cdot \boldsymbol{\nabla}\psi = \boldsymbol{e}_r \cdot \boldsymbol{\nabla}\phi = 0, \quad \rho_e = 0, \quad p = 0, \quad \text{on } \Gamma_r, \tag{2.14}$$

$$V = 0, \quad \boldsymbol{u} = 0, \quad \boldsymbol{e}_z \cdot \boldsymbol{\nabla}\psi = \boldsymbol{e}_z \cdot \boldsymbol{\nabla}\phi = 0, \quad \rho_e = 0, \quad p = 0, \quad \text{on} \Gamma_u, \tag{2.15}$$

$$\boldsymbol{e}_r \cdot \boldsymbol{E} = 0, \quad \frac{\partial(\boldsymbol{e}_z \cdot \boldsymbol{u})}{\partial r} = \boldsymbol{e}_r \cdot \boldsymbol{u} = 0, \quad \boldsymbol{e}_r \cdot \boldsymbol{\nabla}\psi = \boldsymbol{e}_r \cdot \boldsymbol{\nabla}\phi = 0, \quad \text{on } \Gamma_l. \tag{2.16}$$

We write the system of equations in dimensionless form using $l_c = R$, $t_c = \mu_l l_c/\gamma$, $u_c = l_c/t_c$, $p_c = \gamma/l_c$, $E_c = Q_o/(4\pi\varepsilon_o l_c^2)$ and $\rho_{e,c} = \varepsilon_o E_c/l_c$ as the characteristic scales

for length, time, velocity, pressure, electric field and volumetric charge, respectively. In particular, the dimensionless forms of the governing equations (2.6)–(2.10a,b) read

$$\widetilde{\nabla} \cdot \tilde{u} = 0, \tag{2.17}$$

$$\frac{1}{Oh^2} \frac{\partial (\frac{\rho}{\rho_l} \tilde{u})}{\partial \tilde{t}} + \frac{1}{Oh^2} \widetilde{\nabla} \cdot \left(\frac{\rho}{\rho_l} \tilde{u}\tilde{u} \right) = -\widetilde{\nabla}\tilde{p} + \widetilde{\nabla} \cdot \left(\frac{\mu}{\mu_l} \left(\widetilde{\nabla}\tilde{u} + \widetilde{\nabla}\tilde{u}^{\mathrm{T}} \right) \right) + \Gamma \tilde{F}_{es} + \tilde{F}_{st}, \tag{2.18}$$

$$\frac{\Pi_1}{\varepsilon_l} \frac{\partial \tilde{\rho}_e}{\partial \tilde{t}} + \frac{\Pi_1}{\varepsilon_l} \widetilde{\nabla} \cdot \left(\tilde{\rho}_e \tilde{u} \right) = -\widetilde{\nabla} \cdot \left(\frac{K}{K_l} \tilde{E} \right) - \frac{\Pi_2}{\varepsilon_l} \tilde{\rho}_e \exp \left(-\Pi_3 \left(1 - \sqrt{\tilde{E}_n^g / \Pi_4} \right) \right), \tag{2.19}$$

$$\varepsilon \widetilde{\nabla}^2 \tilde{V} + \widetilde{\nabla}\tilde{V} \cdot \widetilde{\nabla}\varepsilon = -\tilde{\rho}_e, \tag{2.20}$$

$$\frac{\partial \phi}{\partial \tilde{t}} + \tilde{u} \cdot \widetilde{\nabla}\phi = \frac{1}{Pe} \widetilde{\nabla}^2 \tilde{\psi}, \quad \tilde{\psi} = \frac{1}{\tilde{\xi}}(\phi^2 - 1)\phi - \tilde{\xi}\widetilde{\nabla}^2 \phi, \tag{2.21a,b}$$

where dimensionless variables are designated with an overtilde. Equations (2.17)–(2.21a,b) include eight dimensionless numbers: Oh, Γ, Π_1, Π_2, Π_3, Π_4, Pe and ε_l. In addition, the ratios ρ_g/ρ_l, μ_g/μ_l and K_g/K_l are nearly zero and $\varepsilon_g \cong 1$ for all liquid/gas combinations. The Ohnesorge number is the ratio between the viscous time scale t_c and the inertial time scale $\sqrt{\rho_l R^3/\gamma}$:

$$Oh = \frac{\mu_l}{\sqrt{\gamma \rho_l R}}, \tag{2.22}$$

and measures the relative importance of viscous and inertial forces. The Taylor number:

$$\Gamma = \frac{\varepsilon_o E_c^2 R}{\gamma} \tag{2.23}$$

measures the relative importance between the electrostatic and capillary stresses. In particular, $\Gamma = 4$ indicates that the droplet is charged at the Rayleigh limit. The Π_1 is the ratio between the electrical relaxation time $t_e = \varepsilon_l \varepsilon_o / K_l$ and the characteristic time scale:

$$\Pi_1 = \frac{t_e}{t_c} = \frac{\varepsilon_l \varepsilon_o \gamma}{K_l \mu_l R}. \tag{2.24}$$

The Π_1 is indicative of the speed at which the charge migrates from the bulk to the surface in an attempt to make the liquid phase equipotential. The dimensionless groups Π_2, Π_3 and Π_4 determine the importance of ion field emission:

$$\Pi_2 = \frac{\varepsilon_l \varepsilon_o k_B T}{K_l h}, \quad \Pi_3 = \frac{\Delta G}{k_B T}, \quad \Pi_4 = \frac{4\pi \varepsilon_o \Delta G^2}{e^3 E_c}. \tag{2.25a–c}$$

Here, Π_2 is the ratio between the electrical relaxation time and the molecular evaporation time $h/k_B T$, Π_3 is the ratio between the ion solvation energy and the molecular thermal energy and Π_4 is the dimensionless characteristic electric field for ion emission, $\tilde{E}^*$. Finally, the Péclet number measures the relative importance of convection and diffusion in the Cahn–Hilliard equation:

$$Pe = \frac{R^3}{\zeta \gamma t_c}. \tag{2.26}$$

For all the numerical cases considered in this study, we make $\zeta = (R\xi)^2/p_c t_c$ (Ding, Gilani & Spelt 2010; Mandal *et al.* 2015), i.e. $Pe = 1/\tilde{\xi}^2$.

Q (nl s^{-1})	I_B (nA)	R (nm)	Oh	Π_1	Π_4
0.153	230.	17.	33.7	9.36×10^{-3}	1.82
0.233	265.	20.5	30.7	7.76×10^{-3}	2.00
0.297	300.	22.2	29.5	7.17×10^{-3}	2.08
0.375	325.	24.6	28.0	6.47×10^{-3}	2.19
0.464	350.	26.9	26.8	5.92×10^{-3}	2.29
0.562	375.	29.2	25.7	5.45×10^{-3}	2.38
0.629	400.	30.2	25.3	5.27×10^{-3}	2.42
0.743	425.	32.4	24.4	4.91×10^{-3}	2.51
0.905	450.	35.6	23.3	4.47×10^{-3}	2.63

Table 1. Flow rates, beam currents and droplet radii of EMI-Im electrosprays (Gamero-Castaño & Cisquella-Serra 2020), together with size-dependent dimensionless numbers for droplets charged 4 % above the Rayleigh limit.

2.2. *Numerical implementation*

Our goal is to study the role of ion field evaporation in the formation of electrosprayed nanodroplets of highly conducting liquids, in particular ionic liquids. To the best of our knowledge, this is the only practical situation in which droplets directly form both above the Rayleigh limit and can field emit ions. The central problem is understanding how ion field emission modifies the sprays of a given liquid at varying flow rate, or equivalently as a function of the droplet radius. We focus on the electrosprays of the ionic liquid EMI-Im because it has been thoroughly studied, e.g. it is known that ion emitted from droplets in flight is a key element of the physics, and that some droplets undergo Coulomb explosions while others emit ions and do not fragment (Gamero-Castaño & Cisquella-Serra 2020). Thus, in all calculations, we use the physical properties of EMI-Im, $\varepsilon_l = 12.2$, $\rho_l = 1520\,\text{kg m}^{-3}$, $\mu_l = 0.032\,\text{Pa s}$, $K_l = 0.74\,\text{S m}^{-1}$ and $\gamma = 0.0349\,\text{N m}^{-1}$. For the gas phase, we use $\varepsilon_g = 1$, $\rho_g = 1\,\text{kg m}^{-3}$, $\mu_g = 10^{-4}\,\text{Pa s}$ and $K_g = 10^{-9}\,\text{S m}^{-1}$. A precise value of the ion solvation energy is not available and we use the estimate $\Delta G = 1.62\,\text{eV}$ (Iribarne & Thomson 1976; Loscertales & Fernández De La Mora 1995; Gamero-Castaño & Fernández De La Mora 2000*a*). In all simulations, we consider an initial charge 4 % above the Rayleigh limit, $Q_o = 1.04 Q_{Ray}$.

Table 1 shows typical flow rates, beam currents and droplet radii of EMI-Im electrosprays (Gamero-Castaño & Cisquella-Serra 2020), together with the values of size-dependent dimensionless numbers (we assume a charge 4 % above the Rayleigh limit). The values of the dimensionless numbers that do not depend on the radius of the droplet are $\Gamma = 4.016$, $\Pi_2 = 906$, $\Pi_3 = 63.1$, $\varepsilon_l = 12.2$ and $Pe = 10^4$ (we use $\xi = R/100$ in all calculations). Note that ion field emission from droplets of highly conducting liquids is characterized by high Ohnesorge numbers (all ionic liquids have high viscosities, comparable or larger to that of EMI-Im, and the droplet radii must be at most a few tens of nanometres to sustain the electric fields needed for significant ion emission) and small Π_1 (the charge is, for all purposes, relaxed on the surface). Therefore, varying the droplet radius for a given ionic liquid at constant excess charge over the Rayleigh limit is equivalent to varying Π_4 while keeping Γ, Π_2, Π_3, Pe and ε_l constant, in the limit $Oh^2 >> 1$ and $\Pi_1 \ll 1$.

We use COMSOL Multiphysics Software to solve the system of equations (Comsol, Inc. 2019). We employ for most equations COMSOL's built-in laminar flow, electrostatics and phase field interface, which uses a finite element solver. The volumetric charge
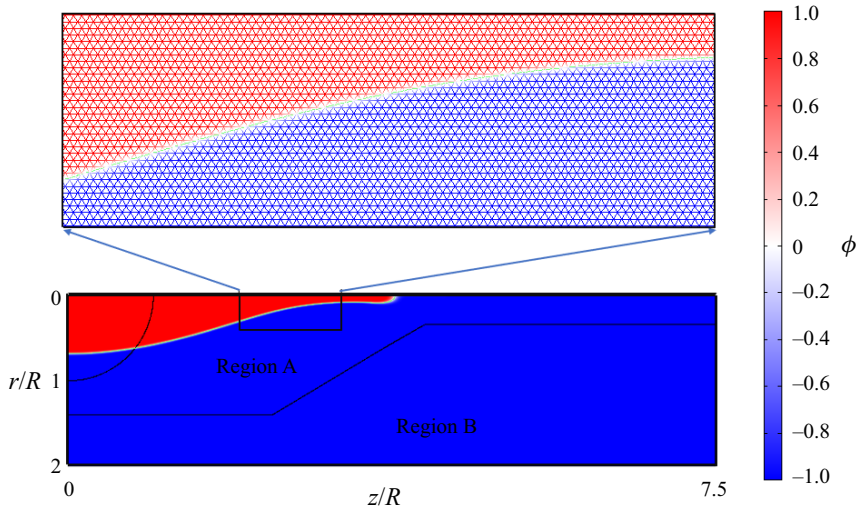
Figure 2. A section of the computational domain along with details of the grid and the variation of the phase variable ϕ.

conservation equation (2.8) cannot be incorporated with built-in interfaces so we use instead the partial differential equation interface. Additionally, we include the electrostatic (2.11) and surface tension (2.12) volumetric forces in (2.7) as forcing terms. The equations are solved in COMSOL's weak formulation framework. The phase variable ϕ is discretized using a cubic-order Lagrange element; $\boldsymbol{u}$, V and ρ_e are discretized using quadratic-order Lagrange elements; and p is discretized using a linear Lagrange element. We use the parallel sparse solver MUMPS for marching the solution in time. MUMPS uses a second-order backward differential formulation scheme with variable time step, computed using the Courant–Friedrichs–Lewy condition (Courant, Friedrichs & Lewy 1967). The maximum time step is set at $\Delta t_{max}/t_c = 0.01$, while typical time steps at the start of the simulation are of the order of 10^{-5}. When needed (e.g. to analyse the results), the position of the surface is computed as the loci where $\phi = 0$ by interpolation. For spatial discretization, we use a triangular grid with grid size h. The computational domain is divided into two regions, as depicted in figure 2. Region A contains the droplet and its grid size is $h = R/64$, while region B has a grid size $h = R/30$. The variation of the phase variable ϕ is depicted in figure 2 along with details of the triangular grid. The diffuse interface thickness is fixed at $\xi = R/100$ (Misra & Gamero-Castaño 2022). The post-processing of the results is performed with the COMSOL–MATLAB interface.

Initially, we impose a homogeneous charge density $\rho_{e,o} = 3\eta Q_{Ray}/(4\pi R^3)$ in Ω_l, with $\eta = 1.04$. The charge is allowed to relax at zero fluid velocity, migrating to the interface to make the droplet equipotential (Misra & Gamero-Castaño 2022). Once the charge relaxes, we compute the deformation of the droplet over time. In most calculations, we use $H = L = 10R$ and have verified that these values do not affect the solution. When calculating the elongation of the jet, we use a longer domain with $H = 14R$. Appendix B provides details about the charge relaxation step and Appendix C presents a grid independence study.
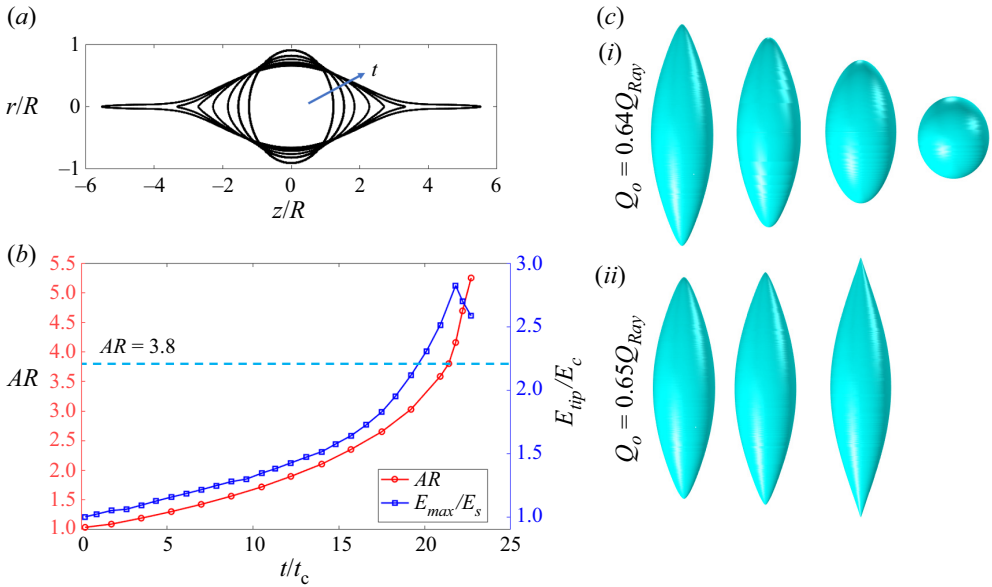
Figure 3. Coulomb explosion of a droplet without ion emission (PRF), with initial charge $1.04Q_{Ray}$, $Oh = 28$ and $\Pi_1 = 0.05$: (*a*) evolution of the droplet's shape with time. The aspect ratios (*AR*) are 1.36, 1.89, 2.43, 3.20, 3.79, 4.79 and 8.41 at increasing time; (*b*) evolution of the aspect ratio and the electric field on vertex $\tilde{E}_{tip}$; (*c*) evolution of the droplet starting right before the critical shape is formed ($AR = 3.68$), when the total charge is reduced to (*c* i) $Q_o = 0.64Q_{Ray}$ and (*c* ii) $Q_o = 0.65Q_{Ray}$.

3. Results and discussions

3.1. *The Coulomb explosion of a droplet in the absence of ion field emission*

This problem has been thoroughly investigated (Burton & Taborek 2011; Collins *et al.* 2013; Garzon *et al.* 2014; Gawande *et al.* 2017) and the comparison with our solution makes it possible to validate the numerical model. In the remainder of the paper, this case is referred to as 'pure Rayleigh fission', PRF. Physically, this scenario corresponds to large droplets with electric fields substantially lower than E^*. For the calculations, we use a droplet with $D = 50$ nm having the physical properties of EMI-Im, with the exception of using a lower electrical conductivity, $K = 0.095$ S m^{-1}, to simplify capturing the evolution. This leads to $Oh \sim 28$ and $\Pi_1 \sim 0.05$.

Figure 3(*a*) shows the evolution of a droplet with $Q_o = 1.04Q_{Ray}$. Initially nearly spherical, the droplet becomes an ellipsoid of increasing aspect ratio. The vertices eventually transition into cusps, which elongate to form jets. We quantify the evolution of the droplet with the aspect ratio, *AR*, defined as the quotient between the spans of the droplet along the axial and radial directions. Figure 3(*b*) shows the aspect ratio and the electric field on the vertices $\tilde{E}_{tip}$, as a function of time. The shape of the droplet just prior to the formation of jets is referred to as the critical shape. Its aspect ratio, $AR \cong 3.82$, is close to the experimental value of 3.7–3.85 for droplets in the Stokes limit (Duft *et al.* 2003; Achtzehn *et al.* 2005; Giglio *et al.* 2008); it also compares well with the values of previous numerical calculations, 3.85–3.87 (Gawande *et al.* 2017, 2020; Giglio *et al.* 2020). Here, $\tilde{E}_{tip}$ reaches its maximum value for an aspect ratio slightly larger than that of the critical shape. The aspect ratio grows rapidly once the jet is formed. Appendix A provides additional comparison with experimental data.

Prior experiments and calculations have shown that the jets are unstable and generate small droplets. The main elongated drop left after the detachment of the progenies relaxes back to a spherical shape, with a charge that is substantially smaller than the original and most of the original mass (Duft *et al.* 2003; Giglio *et al.* 2008). An accurate calculation of the dynamics of the jet breakup and the formation of droplet progenies requires a higher grid resolution than employed in this article (the capture of radial features is limited by our choice of interface thickness, $\xi = R/100$), but doing so increases the computational cost dramatically. Although we do not capture the entire fission process, we can estimate the amount of charge that a parent droplet must shed to become stable. Starting with the shape at $AR = 3.68$ (just prior to the formation of the critical shape), we progressively reduce the charge and observe the evolution to discern whether the droplet develops the jets or goes back to the spherical shape. Figure 3(*c*) illustrates this approach: starting with a shape $AR = 3.68$, if the charge is made to be $Q_o = 0.65Q_{Ray}$, the droplet still forms a jet and is unstable. Conversely, if the charge is slightly reduced to $Q_o = 0.64Q_{Ray}$, the aspect ratio of the droplet decreases and it becomes spheroidal. This suggests that a droplet charged at the Rayleigh limit will shed 36 % of its charge in a Coulomb explosion. Duft *et al.* (2003) and Giglio *et al.* (2008) report an experimental charge loss of 33 %, which is in good agreement with our prediction. A recent equipotential model predicts a charge loss of roughly 39 % (Gawande *et al.* 2017). There is a variation of the fraction of lost charge reported in the literature, which is likely due to viscosity and conductivity effects. For example, for low viscous de-ionized water droplets ($Oh = 0.023$), the critical shape is achieved at $AR = 2.7$–2.9 and a charge loss of roughly 20 % has been measured (Giglio *et al.* 2020), whereas experiments in the Stokes limit ($Oh \gg 1$) report a charge loss of 33 % (Duft *et al.* 2003; Achtzehn *et al.* 2005; Giglio *et al.* 2008).

3.2. *Droplet charged above the Rayleigh limit with ion field emission*

The simulation of a droplet charged above the Rayleigh limit including ion field emission (labelled as WFE, 'with field emission') is motivated by the experimental studies of Gamero-Castaño & Cisquella-Serra (2020), Miller *et al.* (2021) and Perez-Lorenzo & Fernández De La Mora (2022), who report substantial ion currents in electrosprays of several ionic liquids. Retarding potential measurements indicate that these ions are emitted from droplets likely to be charged above the Rayleigh limit. Our simulations reveal three distinct outcomes depending on the initial size of the droplet.

3.2.1. *Small radius regime, region I*

Sufficiently small droplets charged above the Rayleigh limit emit ions from the spherical and spheroidal shapes. Figure 4 shows the evolution of droplets with diameters of 10 and 20 nm charged 4 % above the Rayleigh limit. The 10 nm droplet undergoes marginal deformation while emitting ions, before becoming a stable sphere. The 20 nm droplet follows a similar path, but undergoes a larger deformation. In either case, the droplet does not develop the cusps preceding the formation of the jets and droplet progenies, i.e. the shedding of charge by ion field emission prevents the Coulomb explosion.

Figure 5(*a*) shows the charge of three ion-emitting droplets with diameters of 10, 15 and 20 nm as a function of time, while figure 5(*b*) shows their aspect ratios together with that of a 50 nm droplet in the PRF regime (without ion emission). The initial charge of all droplets is 4 % above the Rayleigh limit. The characteristic time for the shedding of charge scales with t_c, while the fraction of the initial charge that is evaporated increases with decreasing droplet diameter. This is to be expected from the dependency of the electric
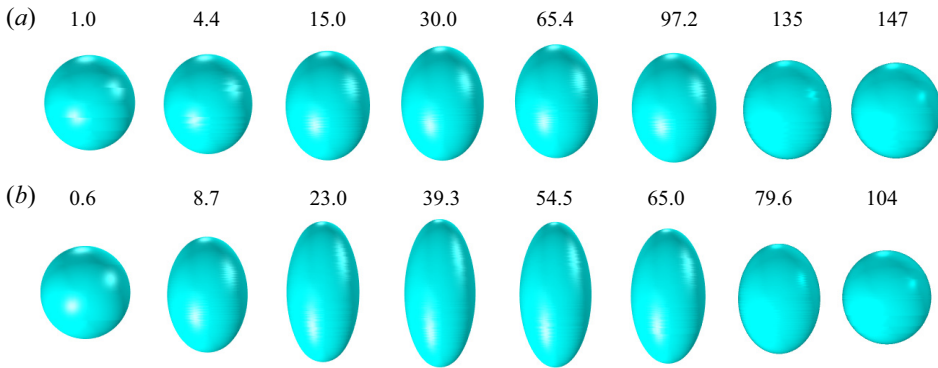
Figure 4. Evolution of EMI-Im droplets emitting ions, with an initial charge $Q_o = 1.04Q_{Ray}$: (*a*) $D = 10$ nm; (*b*) $D = 20$ nm. The times t/t_c for each snapshot are shown above the drops.
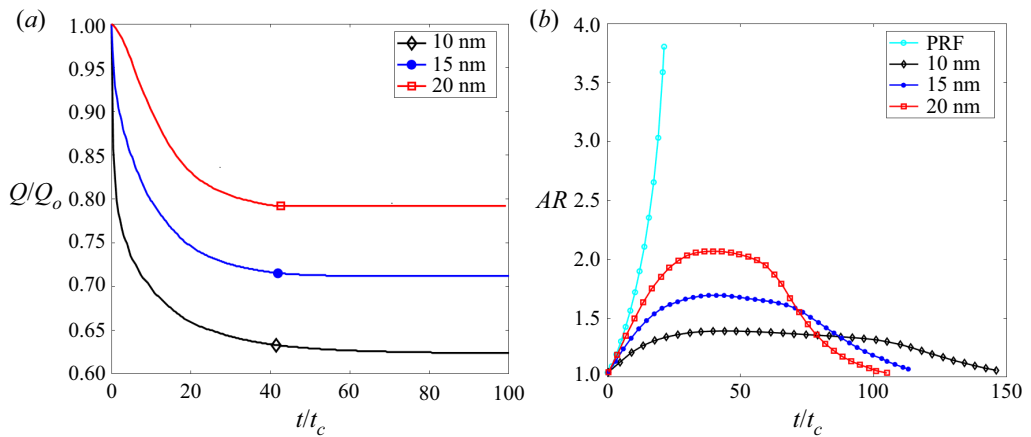

Figure 5. EMI-Im droplets with different diameters emitting ions (initial charge $Q_o = 1.04Q_{Ray}$): (*a*) evolution of the charge held by the droplet; (*b*) evolution of the aspect ratio and comparison with that of a droplet in the PRF regime (without ion emission).

field on the diameter of a droplet at the Rayleigh limit, (1.1*a*,*b*). Note that as the droplets emit ions, their aspect ratios increase. The droplets remain quasi-equipotential during the deformation, and the electric field on the surface scales with the inverse of the square of the local radius of curvature. Thus, as the aspect ratio of the droplet increases, ion emission preferentially takes place from the vertices of the ellipsoid. The aspect ratios of the droplets plateau once ion emission becomes negligible, a larger droplet exhibits a larger deformation. From this state of maximum deformation, the droplet falls back to the spherical shape, now stable with a constant charge that can be significantly smaller than the Rayleigh limit. The 10, 15 and 20 nm droplets lose 38 %, 28 % and 20 % of their initial charge, respectively. Given the substantial charge loss, the electric stress at the vertices of the ellipsoid is insufficient to form the cusps and jets characteristic of a Coulomb explosion.

Figure 6 shows the evolution of the normal component of the electric field at the vertex of the droplet. In all cases, the electric field levels off near $E_n^g/E^* \approx 0.76$ when ion emission is significant, i.e. $0.76 \times E^*$ is the effective value of the electric field during ion emission: when the electric field is slightly above $0.76 \times E^*$, the high intensity of the
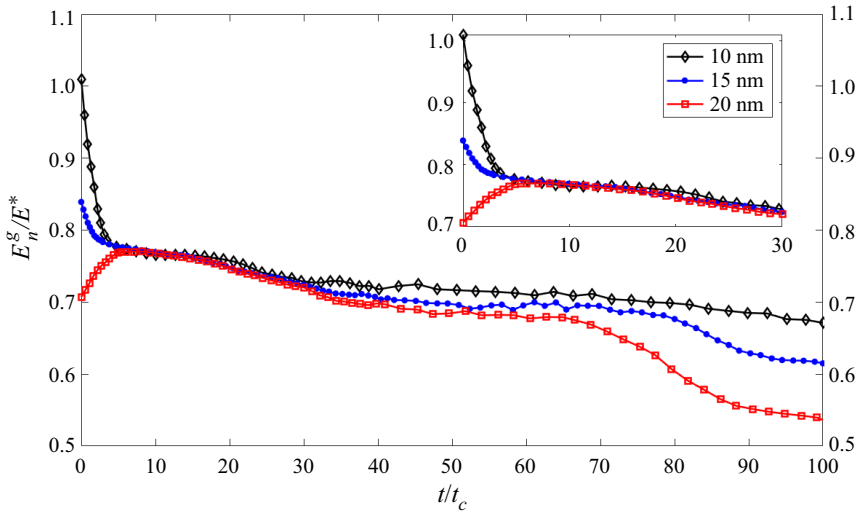
Figure 6. Evolution of the outer electric field on the vertices of EMI-Im droplets emitting ions, with an initial charge $Q_o = 1.04 Q_{Ray}$.

ion flux (see exponential dependency of the emitted current on the electric field) rapidly reduces the charge of the droplet, bringing down the electric field to this effective value for ion emission; and ion emission is negligible if the electric field is slightly below $0.76 \times E^*$. The initial electric field for the two smaller droplets is above the effective value and therefore both of them are characterized by an initial brief period of intense ion emission. Conversely, the electric field for the larger droplet, $D = 20$ nm, is initially below the effective value and, although the droplet emits ions from its initial state, it needs to deform to reach the effective electric field and increase ion emission. The total charge evaporated during the time in which the electric field is approximately constant is significant for all three droplets (see figure 5*a*). The freezing of the electric field during ion emission was previously observed in the experiments by Loscertales & Fernández De La Mora (1995). Finally, note that the evolution of the electric field in figure 6 may exhibit, at times, an unphysical wiggle. This artefact is due to how we evaluate the electric field for the purpose of making the plot: E_n^g is defined at the surface, which in general does not coincide with the position of the nodes in the computational grid. Thus, we compute E_n^g by interpolating the values of the electric field between two nodes, in a region where the electric field and the volumetric charge exhibit large gradients. This causes the wiggle. A more accurate way of computing E_n^g would consist of using more nodes in the grid to fit the values of the electric field to appropriate analytical functions and determining the value at the surface from the fitting. However, note that this is only important for plotting purposes, because E_n^g is not a variable used in the calculations (the surface and therefore the electric field at the surface are not part of the calculations in the phase field method).

3.2.2. *Medium radius regime, region II*

In this case, the initial electric field on the surface of the spherical droplet is insufficient to emit ions. Similarly to the PRF case, the unstable droplet deforms into an ellipsoid of increasing aspect ratio at constant charge. As the electric field near the vertices of the ellipsoid increases, it eventually becomes high enough to promote significant ion emission, discharging the droplet and preventing the Coulomb explosion.
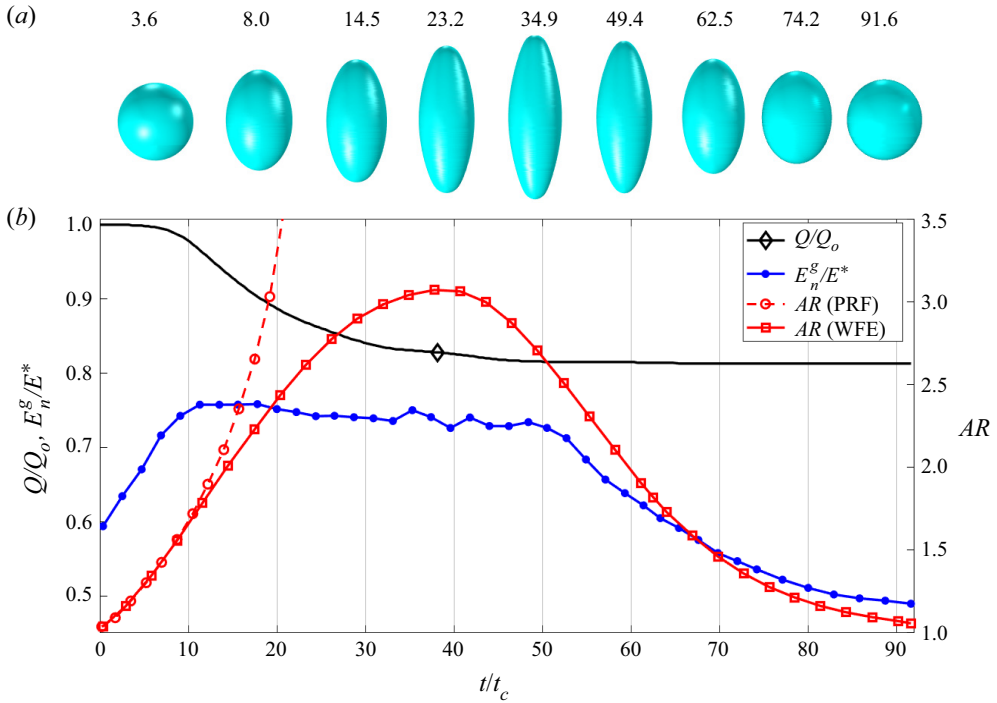
Figure 7. Results for a $D = 30$ nm droplet with initial charge $Q_o = 1.04Q_{Ray}$, including ion emission: (*a*) evolution of the droplet's shape (t/t_c is shown above the drops); (*b*) evolution of the aspect ratio (for comparison, we also include the aspect ratio of a PRF droplet), charge and outer electric field at the vertices of the droplet.

Figure 7 displays the evolution of a $D = 30$ nm droplet initially charged 4 % above the Rayleigh limit. Figure 7(*a*) shows the droplet deforming into an ellipsoid of increasing aspect ratio, reaching a maximum deformation, and going back to a sphere without developing the cusps and jets typical of a Coulomb explosion. Figure 7(*b*) shows the aspect ratio, the charge and the electric field at the vertices of the droplet as functions of time. Initially, the trend for the aspect ratio coincides with that for the PRF case because the electric field near the vertices is insufficient to support ion emission. However, as the electric field at the vertices reach a critical value at $t/t_c \sim 10$, the droplet begins to shed charge and the aspect ratios of the PRF and WFE droplets start to separate. The aspect ratio of the WFE droplet, rather than accelerating, reaches a maximum at $t/t_c \sim 38$. By this time, the droplet has lost 17.3 % of its charge by ion field emission, which takes place at nearly constant electric field, $E_n^g/E^* \sim 0.76$–0.77. Most of the ion emission occurs up to the maximum of the aspect ratio. Minor ion emission continues to take place as the droplet relaxes to the stable spherical configuration, being negligible for $t/t_c \gtrsim 54$. Because of the reduced electrification, the cusps and jets never develop, i.e. the Coulomb explosion is suppressed.

Figure 8 shows the evolution for a larger droplet, $D = 40$ nm, also charged 4 % above the Rayleigh limit. Although, in this case, ion emission is triggered at a later time due to the lower initial electric field, it also suppresses the Coulomb explosion. The droplet follows the PRF trend for a longer time due to the later onset of ion emission. At $t/t_c \sim 14$, the electric field at the vertices is sufficiently high to trigger ion emission
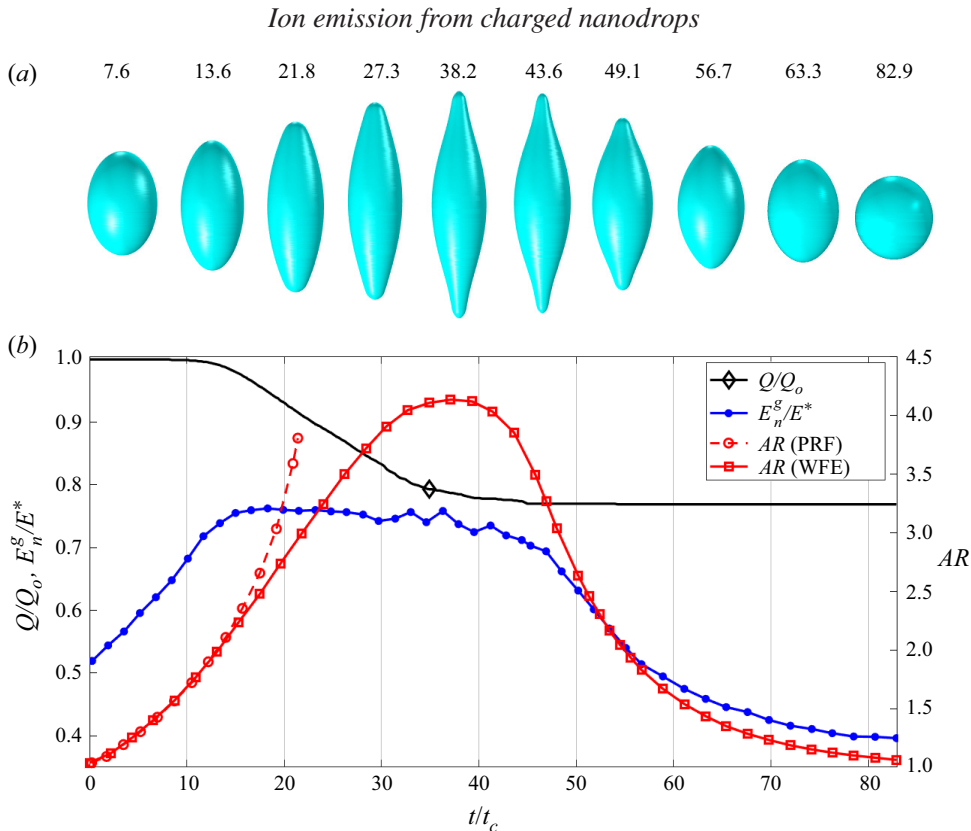
958 A32-14

Figure 8. Same as figure 7 for a larger droplet, $D = 40$ nm.

($E_n^g/E^* \sim 0.76$–0.77). The droplet starts to emit charge and the aspect ratio separates from the PRF droplet. Note that the vertices of the ellipsoid are almost transitioning into cusps when the aspect ratio plateaus at $t/t_c \sim 38.2$. Interestingly, the aspect ratio exceeds 3.8, which is the critical aspect ratio for the PRF case. The larger 40 nm droplet sheds a higher fraction of its initial charge than the 30 nm droplet, $\sim 24\,\%$ and $\sim 19\,\%$, respectively.

These findings (regions I and II) provide an alternative scenario for ion emission to that proposed by previous authors who assume that it takes place from a spherical droplet only when its initial electric field E_o can promote significant ion emission while being lower than that associated with the Rayleigh limit, $E^* \leq E_o < E_{Ray}$ (Iribarne & Thomson 1976; Labowsky 1998; Labowsky *et al.* 2000). Furthermore, they confirm the qualitative arguments put forward by Gamero-Castaño & Fernández de la Mora (2000) and Gamero-Castaño & Cisquella-Serra (2020), namely that droplets undergoing Coulomb explosions may emit ions from areas of high electric fields, suppressing the fission process.

3.2.3. *Large radius regime, region III*

Lastly, we discuss relatively large droplets charged above the Rayleigh limit, specifically in the diameter range 45–100 nm. The unstable droplet evolves into an ellipsoid, developing cusps and jets. Ion emission may take place from the vertices and the jets, but cannot prevent the Coulomb explosion. Both ion emission and droplet progenies reduce the charge of the droplet.
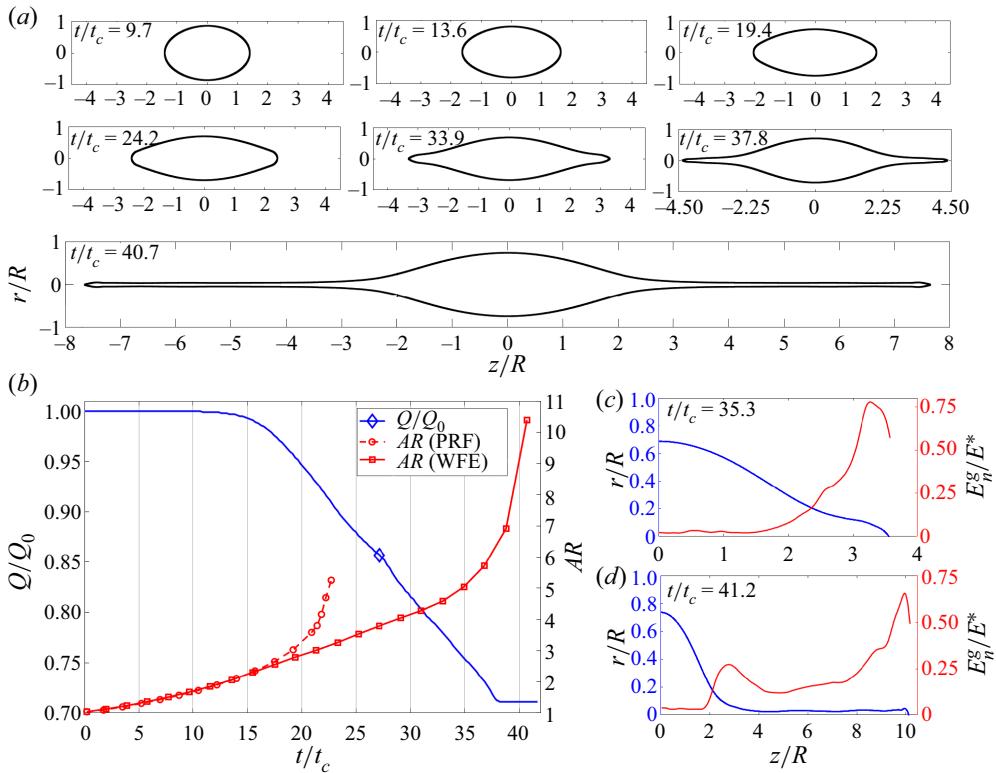
Figure 9. Simulation of a $D = 45$ nm droplet with initial charge $Q_o = 1.04 Q_{Ray}$, undergoing Coulomb explosion and ion field emission (WFE): (*a*) droplet shape at different times; (*b*) evolution of the charge and aspect ratio of the droplet; (*c*) profile of the droplet's surface and outer electric field at $t/t_c = 35.3$; (*d*) profile of the droplet's surface and outer electric field at $t/t_c = 41.2$.

Figure 9 shows a simulation for a $D = 45$ nm droplet initially charged 4 % above the Rayleigh limit. The evolution of the shape is qualitatively similar to the PRF case: the spherical droplet becomes an ellipsoid of increasing aspect ratio; it develops cusps at the vertices; and the cusps move away from the centre forming jet-like extensions. Ion emission is negligible until $t/t_c = 15.4$. Beyond this time, the electric field at the vertices is high enough to emit ions, lowering the charge of the droplet and slowing the speed at which the aspect ratio increases. However, the shedding of charge does not impede the formation of cusps and jets, depicted in the droplet profiles at $t/t_c = 33.9$, 37.8 and 40.7. It is interesting that electric fields high enough to evaporate ions only develop at the vertices of the spheroid and at the cusps. At $t/t_c \gtrsim 38$, the electric field at the cusps is not sufficient to continue the emission of ions and the net charge of the droplet remains constant. The jets continue to elongate, and we assume that natural instability will lead to their breakup and the formation of droplet progenies. Overall, the droplet sheds roughly 28–29 % of its charge by ion emission. Profiles of the electric field along the surface at different times are shown in figure 9(*c*), $t/t_c = 35.3$, and figure 9(*d*), $t/t_c = 41.2$. At the earlier time, the electric field increases towards the cusps, where it reaches a value consistent with significant ion evaporation, $E_n^g/E^* = 0.76$–0.77. The profile for $t/t_c = 41.2$, i.e. for a situation with developed jets, shows two distinct maxima. The lower maximum occurs near the transition region of the jet $z/R \sim 2.6$–2.7, whereas the larger electric field occurs
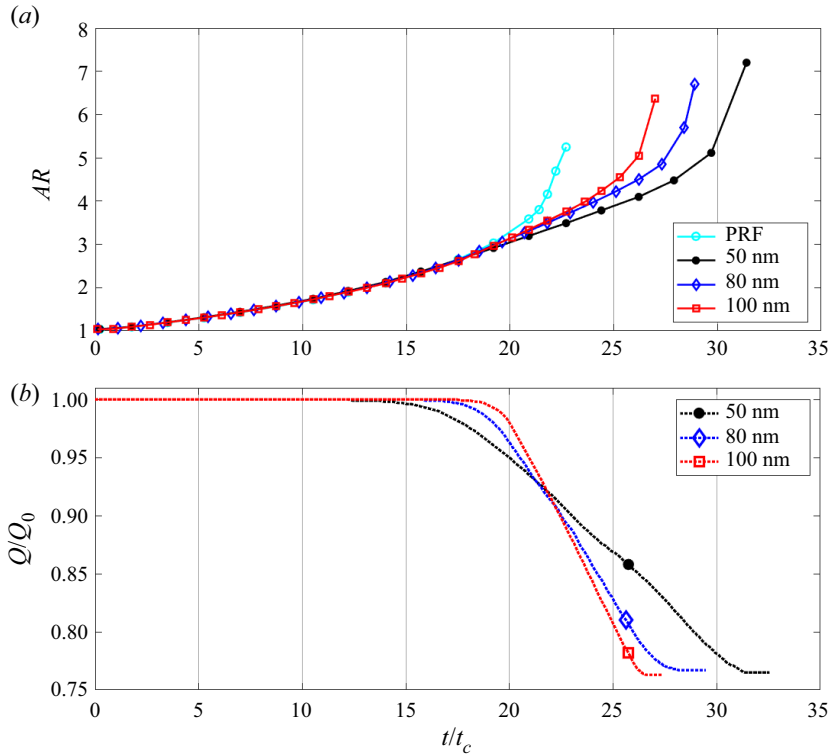
958 A32-16

Figure 10. Results for droplets with diameters of 50, 80 and 100 nm: (*a*) evolution of the aspect ratio and comparison with that of a PRF droplet; (*b*) evolution of the droplet's charge.

at the tip of the jet. The value of the latter is $E_n^g/E^* \sim 0.67$, i.e. insufficient to trigger significant ion emission, as reflected by the constancy of the charge carried by the droplet at this time.

Figure 10 shows that larger droplets (diameters of 50, 80 and 100 nm) behave similarly to the droplet with a diameter of 45 nm: ion emission is absent from the initial spherical configuration; the deformation follows the PRF path until the electric field at the vertices is sufficient to evaporate ions; and ion emission does not prevent the formation of jets and the Coulomb explosion. The aspect ratio curves match the PRF trend for most of the evolution; however, the three curves depart from the PRF trend before the critical shape forms. This is due to the onset of ion emission from the vertices before the formation of cusps. Larger droplets follow the PRF path more closely and we expect that ion emission never occurs for sufficiently large droplets. The three droplets loose a similar fraction of their charge by ion emission, approximately 24 %, but the loss is more gradual and starts at an earlier time for the smaller droplet. As in the case of the $D = 45$ nm droplet, ion emission eventually ceases at a time when the jet is still elongating, suggesting that the droplets will undergo Coulomb explosions and produce droplet progenies.

In our calculations, the large droplets that emit ions during a Coulomb explosion lose approximately 24 % of their charge by ion emission. Since the total charge loss of PRF droplets is approximately 36 %, we estimate that the droplets in region III lose approximately 16 % of the charge in the form of droplet progenies (considering that $Q_o = 1.04Q_{Ray}$). The rationale behind this estimate is that the shape of the ion-emitting droplet at the time the jets form is similar to the critical shape of the PRF droplet and
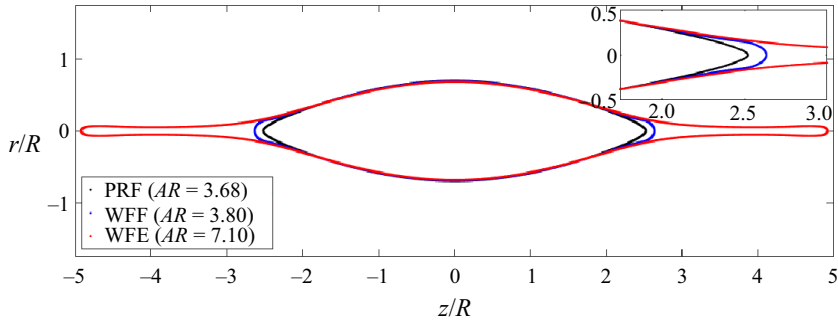
Figure 11. Profiles of a $D = 100\,\text{nm}$ droplet undergoing Coulomb explosion with ion emission ($AR = 3.80$ and $AR = 7.10$) and comparison with a PRF droplet near the critical shape ($AR = 3.68$).

therefore they both must lose a similar amount of charge to fall back to the stable spherical configuration (this is the argument made by figure 3*c*). The comparison of the droplet shapes shown in figure 11 supports this estimate: the shape of the PRF droplet right before the critical point ($AR = 3.68$, see figure 3*a*) matches the profile of the $D = 100\,\text{nm}$ droplet well, with slight differences near the vertices. Our estimate that large droplets lose approximately 24 % of their charge by ion emission agrees with the findings of Perez-Lorenzo & Fernández De La Mora (2022), who hypothesize that the majority of ions observed in the electrosprays of EMI-FAP are emitted from nanodroplets undergoing Coulomb explosions. The experiments of Perez-Lorenzo & Fernández De La Mora (2022) show that approximately 20–25 % of the total current is emitted in the form of ions, a value not far from our prediction; furthermore, the average diameter of the primary droplets of EMI-FAP in these experiments is estimated to be near 90 nm, i.e. within regime III.

Figure 12(*a*) shows the total charge emitted from EMI-Im droplets in regions I and II by ion emission as a function of the diameter of the droplet. Figure 12(*b*) plots the electric field on the surface of a spherical droplet charged 4 % above the Rayleigh limit, as a function of the diameter of the droplet (the electric field is normalized with the characteristic value for ion emission E^*); figure 12(*b*) also shows the domains of regions I, II and III. Here, $E_c/E^* \gtrsim 0.77$ in region I and, therefore, ion emission is significant from the initial spherical configuration. Although the droplet deforms into an ellipsoid of increasing aspect ratio, ion emission prevents the formation of cusps and the Coulomb explosion and, once enough charge is shed, the droplet goes back to a spherical shape with a charge below the Rayleigh limit. Region II is characterized by droplets with initial electric fields in the range $0.47 \lesssim E_c/E^* \lesssim 0.77$. The initial electric field is not sufficient to trigger ion emission; however, as the droplet deforms and the curvature at the vertices becomes large enough, ions are emitted from this small region, discharging the droplet and preventing the formation of cusps and the Coulomb explosion. The droplet subsequently retracts to the stable spherical configuration below the Rayleigh limit. Region III is characterized by initial electric fields $E_c/E^* \lesssim 0.47$. These droplets develop cusps and jets, and hence undergo Coulomb explosions yielding droplet progenies. These droplets lose a significant fraction of their charge by ion emission from their vertices and jets; however, the reduction of charge does not prevent the Coulomb explosion and the formation of droplet progenies.

We can estimate the maximum diameter of the droplet, D_{max}, for which ion emission is significant, i.e. the diameter separating region III from the PRF regime. Figure 3(*b*) shows that, for EMI-Im droplets in the PRF regime charged near the Rayleigh limit, the maximum value of the electric field, $E_{tip}/E_{Ray} \cong 2.83$, occurs at the cusps when the aspect ratio is
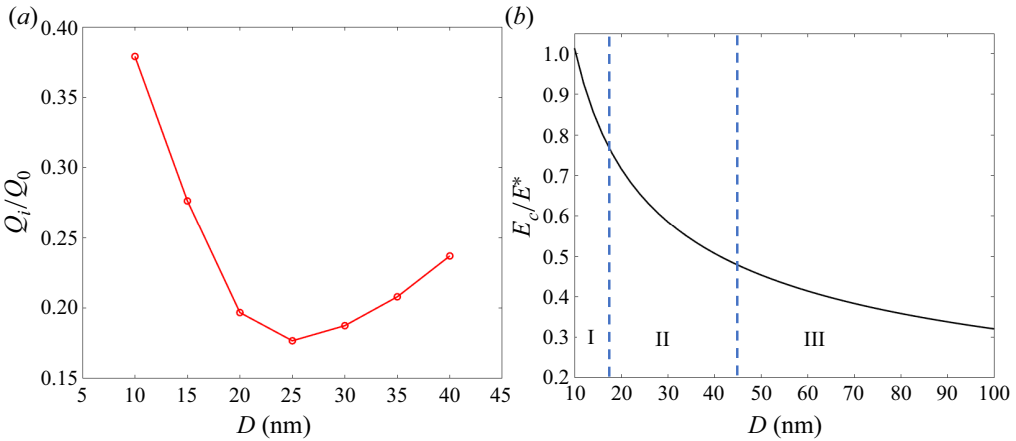
Figure 12. (*a*) Charge lost by ion emission (Q_i) for droplets in regions I and II; (*b*) electric field on the surface of a spherical droplet charged 4 % above the Rayleigh limit, as a function of the diameter of the droplet and ranges of regions I, II and III.

slightly larger than that of the critical shape. Furthermore, ion emission is significant only when $E_{max}/E^* \geq 0.76$. These two relations can be combined to obtain D_{max} (considering droplets 4 % above the Rayleigh limit):

$$D_{max} = \frac{\gamma}{2\varepsilon_o^3} \left(\frac{e^3}{0.26\pi \Delta G^2} \right)^2 . \tag{3.1}$$

Here, $D_{max} = 140$ nm for the conditions used in our numerical calculations. We expect droplets with larger diameters to be in the PRF regime.

We have used an initial charge 4 % over the Rayleigh limit or equivalently, $\Gamma = 4.016$, in all simulations. A higher initial charge excess should have a minor effect on the size windows of regions I, II and III because although ions would be emitted earlier during the deformation of the droplet, the exponential nature of the ion emission law fixes the maximum electric field at a precise fraction of E^*. The amount of charge emitted from a droplet of a given radius with initial charge ηQ_{Ray} will increase with the initial charge and should approximately be that of the droplet charged 4 % over the Rayleigh limit plus $(\eta - 1.04)Q_{Ray}$. Furthermore, using a small charge excess over the Rayleigh limit is representative of practical conditions: for example, charged droplets in aerosols reach the Rayleigh limit by evaporation of the liquid phase at constant charge, i.e. Q_o/Q_{Ray} increases towards 1; and the charged nanodroplets produced during the jet breakup of an electrospray are, at most, slightly charged above the Rayleigh limit, because the breakup process distributes the charge and mass of the jet among neighbouring droplets to minimize the excess charge (Misra & Gamero-Castaño 2022).

4. Conclusions

We have developed an electrohydrodynamic phase field model to study the coupling of ion emission and Coulomb explosion in charged liquid droplets. The model accounts for the finite electric conductivity of the liquid. We draw the following major conclusions from the current study.

(i) Highly viscous droplets charged slightly above the Rayleigh limit emit roughly 36 % of their charge in the form of smaller droplet progenies. This analysis does not take

into account ion field emission and, therefore, is valid for relatively large droplets where the electric field on the surface is not sufficient to support ion emission. For the EMI-Im droplets and conditions considered in the current article, we expect droplets with diameter $D > 140$ nm to follow this trend.

(ii) Ion field emission suppresses Coulomb explosions in droplets that are charged above the Rayleigh limit and are sufficiently small ($D < 45$ nm in our simulations with EMI-Im droplets). Between 20 and 40 % of the initial charge of the droplet is shed by ion emission (we assume an initial charge 4 % above the Rayleigh limit).

(iii) There is an intermediate size range ($45 \lesssim D \lesssim 100$ nm in our simulations with EMI-Im droplets) in which droplets charged above the Rayleigh limit undergo Coulomb explosions, and also emit ions from the vertices and jets of the deforming droplet. We find that approximately 24 % of the initial charge of the droplet is shed by ion emission and estimate that roughly 15–16 % is lost in the form of droplet progenies. This prediction matches well the experiments and analysis of Perez-Lorenzo & Fernández De La Mora (2022).

(iv) Ion emission freezes the value of the electric field in areas where emission is significant. We quantify this value at $E_n^g/E^* \sim 0.76$–0.77.

The continuum approach and the leaky dielectric model have been successful in reproducing Coulomb explosions in the past (Giglio *et al.* 2008; Gawande *et al.* 2017, 2020; Giglio *et al.* 2020). However, these prior studies compare numerical results with experimental data for droplets 10–50 μm in diameter (Duft *et al.* 2003; Achtzehn *et al.* 2005; Giglio *et al.* 2008). Ion emission is relevant only in nanometric droplets and, in these systems, the continuum approximation as well as key assumptions of the leaky dielectric model such as constant electrical conductivity may be less accurate. However, we note that molecular dynamic simulations of ion emission and Coulomb explosions in droplets with diameter less than 10 nm (Luedtke *et al.* 2008) show good qualitative agreement with our calculations. Moreover, recent continuum studies of ion emission from Taylor cones provide confidence in our treatment of this problem (Higuera 2008; Coffman *et al.* 2016, 2019; Gallud & Lozano 2022). Regarding the validity of the leaky dielectric model, it has been shown that this formulation accurately reproduces the similar problem of cone-jets (Gamero-Castaño & Magnani 2019). However, we plan to improve the present model by using an electrokinetic formulation, thus relaxing the assumption of a constant electrical conductivity.

Author ORCIDs.
 Manuel Gamero-Castaño https://orcid.org/0000-0003-2866-2113.

Appendix A. Additional validation of Coulomb explosion calculation

Figure 13 shows a comparison between the actual shape of an ethylene glycol droplet undergoing a Coulomb explosion (second snapshot of figure 4 in Achtzehn *et al.* 2005) ($Oh > 1$) and the critical shape computed with the model ($Oh = 28$, $\Pi_1 = 0.05$).
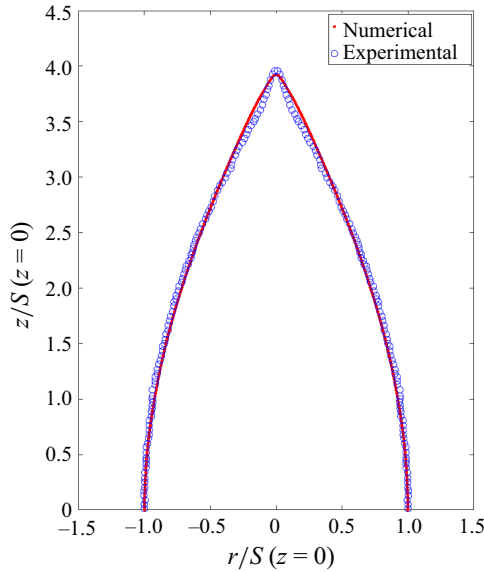
Figure 13. Comparison between the critical shapes of droplets: computed with the model (red) and experimental profile for an ethylene glycol droplet undergoing a Coulomb explosion reported by Achtzehn *et al.* (2005) (blue circles).

ImageJ software was used to extract the experimental profile (Abràmoff, Magalhães & Ram 2019; Misra 2020). The resolution of the image of Achtzehn *et al.* (2005) is not high enough to accurately extract the profile of the jet emitted from the vertex. The comparison shows good agreement between the numerical and experimental profiles, and a good prediction of the critical aspect ratio. The computed semi-cone angle is between $26°$ and $28.5°$ for times near the formation of the critical shape, in agreement with prior numerical results (Betelú *et al.* 2006; Fontelos, Kindelán & Vantzos 2008; Gawande *et al.* 2017; Wang, Ma & Siegel 2019; Gawande *et al.* 2020) and values near $30°$ observed in experiments (Duft *et al.* 2003; Achtzehn *et al.* 2005; Giglio *et al.* 2008).

Perfectly conducting droplets form a conical singularity at the vertices due to the absence of tangential electric stress (Betelú *et al.* 2006; Fontelos *et al.* 2008; Gawande *et al.* 2017). The formation of a conical singularity in perfectly conducting droplets is self-similar with the tip curvature and tip velocity scaling as $l_c\kappa_{tip} = O(\tau^{-\alpha})$ and $w_{tip}/u_c = O(\tau^{\alpha-1})$, respectively, where $l_c\kappa_{tip}$, w_{tip}/u_c are the dimensionless curvature and axial velocity of the tip (Fontelos *et al.* 2008), and $\tau = (t_s - t)/t_c$ is the dimensionless time to singularity formation (at $t = t_s$, singularity occurs). While the singularity never arises in droplets with finite conductivity, Wang *et al.* (2019) realized that if the scaling laws for perfectly conducting droplets are true, then $\tau \sim 1/t_c\kappa_{tip}w_{tip}$. Since w_{tip} and κ_{tip} are accurately determined from the simulation, we can have a prediction for τ, and use the numerical solution to compare the scalings for the tip curvature and the velocity near the formation of the critical shape in droplets with finite electrical conductivity.

Figure 14(*a,b*) depict the dimensionless tip curvature and axial velocity respectively for $Oh = 28$ and $\Pi_1 = 0.004$. The last time stamp in these plots coincides with the critical shape depicted in figure 13. Figure 14(*c*) depicts the tip curvature and velocity as functions of $1/t_c\kappa_{tip}w_{tip}$, similarly to the analysis by Wang *et al.* (2019). The asymptotes are also fitted for each of the cases near the formation of critical shape. The fitting yields $\alpha \sim 0.7$–0.71. Interestingly, Fontelos *et al.* (2008) find $\alpha \sim 0.72$ for conducting droplets in the presence of an external electric field (the semi-cone angle in this case is $27.5°$).
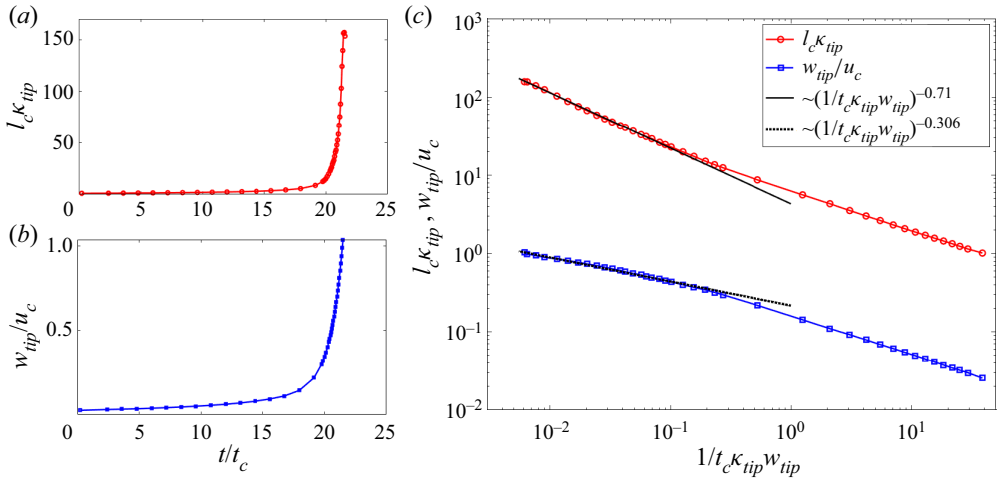
Figure 14. Results for $Oh = 28$, $\Pi_1 = 0.05$: (*a*) dimensionless tip curvature $l_c\kappa_{tip}$ as a function of time; (*b*) tip velocity w_{tip}/u_c as a function of time; (*c*) variation of $l_c\kappa_{tip}$ and w_{tip}/u_c with $1/t_c\kappa_{tip}w_{tip}$.

Wang *et al.* (2019) obtained $\alpha = 0.71$ and a semi-cone angle of $21°$–$24°$ with an electrokinetic model.

Appendix B. Charge relaxation and jump of the electric field across the surface

We next compare the numerical and analytical solutions for the relaxation of an initial homogeneous volumetric charge density ρ_{eo} in the droplet. The migration of charge in the bulk is governed by the charge conservation equation:

$$\frac{\partial \rho_e}{\partial t} + \boldsymbol{\nabla} \cdot (\rho_e \boldsymbol{u}) = -\boldsymbol{\nabla} \cdot (KE), \tag{B1}$$

which can be derived starting from the Poisson–Nernst–Planck (PNP) equation for charged species (Saville 1997) and assuming constant electrical conductivity, negligible diffusion current and fully dissociated salts. For further details of this derivation, see Saville (1997), Herrada *et al.* (2012) and Gañán-Calvo *et al.* (2018); an excellent discussion of its assumption is provided by Ganán-Calvo *et al.* (2016).

Assuming constant electrical conductivity and zero velocity, the charge conservation equation simplifies to

$$\frac{\partial \rho_e}{\partial t} = -K\boldsymbol{\nabla} \cdot E = -K\frac{\rho_e}{\varepsilon_l \varepsilon_o}, \tag{B2}$$

and the charge density is given by

$$\rho_e(t) = \rho_{eo} \exp\left(\frac{-t}{t_e}\right) \quad \text{in } \Omega_l. \tag{B3}$$

When the charge has fully migrated to the surface, the droplet is equipotential and the electric field is given by

$$\frac{E(r)}{E_s} = \begin{cases} 0, & \dfrac{r}{R} < 1 \\ \left(\dfrac{R}{r}\right)^2, & \dfrac{r}{R} \geq 1, \end{cases} \tag{B4}$$
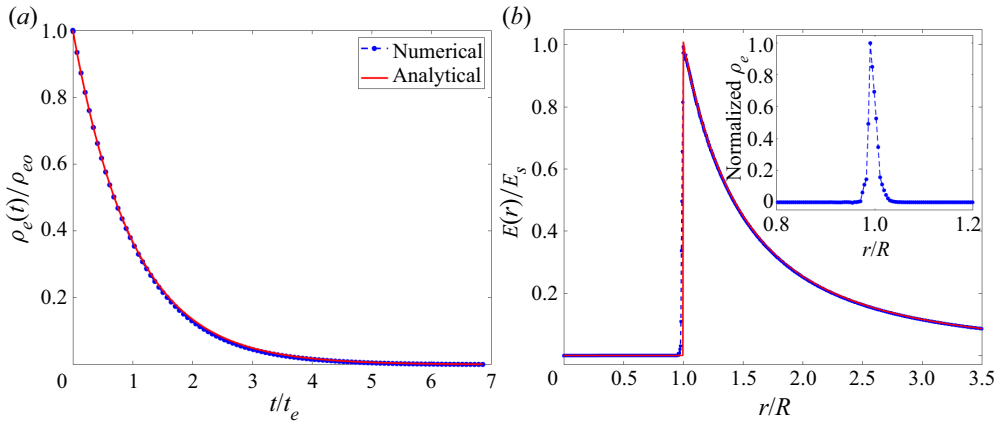
Figure 15. (*a*) Decay of the volumetric charge density inside the droplet (analytical and numerical solutions); (*b*) jump of the electric field across the surface of the droplet upon charge relaxation (analytical and numerical solutions). Inset shows the distribution of the volumetric charge.

where r is the radial spherical coordinate and $E_s = Q/(4\pi\varepsilon_o R^2)$ is the electric field on the surface of the droplet.

Figure 15(*a*) shows the decay of the volumetric charge density inside the droplet computed both analytically and with the model. Figure 15(*b*) shows the spatial variation of the electric field once the charge has relaxed to the surface, both computed with the model and (B4). The inset shows the variation of the volumetric charge. While the phase field method relies on the continuous variation of the phase variable (ϕ), the method accurately captures the jump in the electric field across the surface.

Appendix C. Grid independence test and overall charge conservation

The numerical discretization should not cause significant charge loses. We next test several grid sizes to verify that charge is conserved in our simulations in the case of a droplet undergoing a Coulomb explosion (the total charge must be constant before the detachment of droplet progenies). We also analyse the sensitivity of the droplet and jet profiles to changes in the resolution of the grid. Among all conditions studied in this article, the smallest jet radii occur in droplets undergoing PRF; therefore, the tests in this appendix are worst-case scenario.

Figure 16 compares several figures of merit for four different grid resolutions in region A ($h = R/128$, $R/96$, $R/64$, $R/42$ and $R/27$). The interface thickness parameter is always set such that $\xi = 0.64h$. Figure 16(*a*) shows the evolution of the aspect ratio with time. Figure 16(*b*) demonstrates that the total charge is conserved well by any of the grid resolutions. Figure 16(*c*) compares the profile of the droplet for the different grid resolutions, while figure 16(*d*) shows the error ϵ in the position of the surface, $S(z)$, relative to the position computed with the grid of highest resolution, $h = R/128$:

$$\epsilon = \left| \frac{S_{128}(z) - S(z)}{S_{128}(z)} \right|. \tag{C1}$$

The largest deviation occurs near the transition region of the jet. For $h = R/64$, the maximum error is roughly 3–4 %. For grid resolutions of $R/128$, $R/96$ and $R/64$, the aspect ratios and the surface profiles reasonably coincide, while the charge is
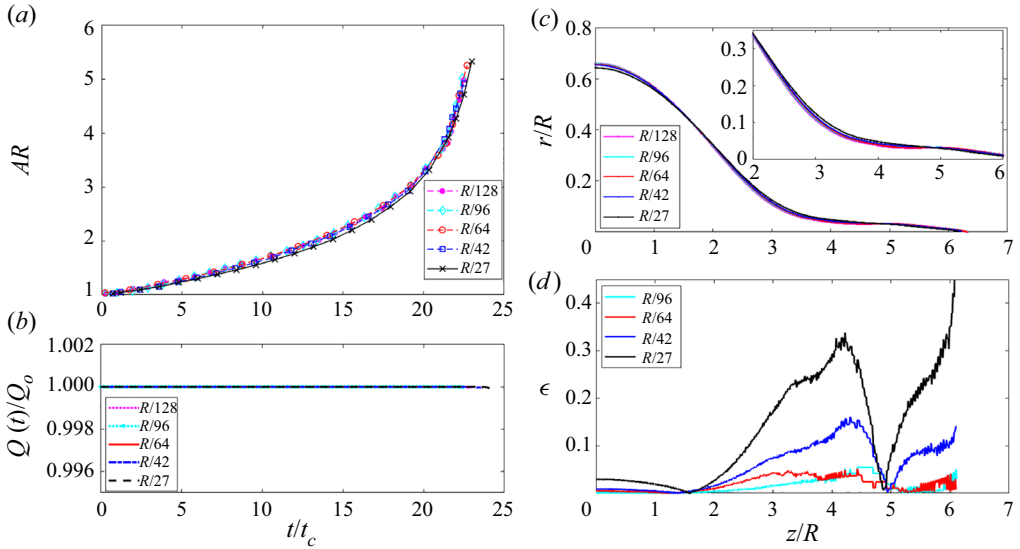
958 A32-23

Figure 16. Grid independence test for a PRF droplet, using grid resolutions $h = R/128, R/96, R/64, R/42, R/27$: (*a*) comparison of the aspect ratio versus time; (*b*) variation of the total charge with time; (*c*) profiles of the droplet once after formation of the jet; (*d*) error in the droplet profiles relative to that calculated with $h = R/128$, (C1).

well conserved. Therefore, to optimize the computational time, we have decided to use the $R/64$ grid in all calculations.

It must be noted that one of the major caveats of using the phase field method in electrohydrodynamic problems is the use of an artificial diffuse interface of finite thickness. With regards to the modelling of jets, the resolution of radial features is limited by the thickness of the diffuse interface ($R/100$ in our case). However, since this study focuses on ion emission from droplets and, as shown in figure 10, ion emission ceases once the jet is formed due to the lowering of the surface electric field, the limitations in the modelling of the jet do not affect the key findings.

REFERENCES

ABRÀMOFF, M.D., MAGALHÃES, P.J. & RAM, S.J. 2019 Image processing with ImageJ. *Biophotonics Intl* **11**, 36–42.

ACHTZEHN, T., MÜLLER, R., DUFT, D. & LEISNER, T. 2005 The Coulomb instability of charged microdroplets: dynamics and scaling. *Eur. Phys. J.* D **34**, 311–313.

ANDERSON, D.M., MCFADDEN, G.B. & WHEELER, A.A. 1998 Diffuse-interface methods in fluid mechanics. *Annu. Rev. Fluid Mech.* **30**, 139–165.

BASARAN, O.A. & SCRIVEN, L.E. 1989 Axisymmetric shapes and stability of isolated charged drops. *Phys. Fluids* **1** (5), 795–798.

BETELÚ, S.I., FONTELOS, M.A., KINDELÁN, U. & VANTZOS, O. 2006 Singularities on charged viscous droplets. *Phys. Fluids* **18** (5), 051706.

BRACKBILL, J.U., KOTHE, D.B. & ZEMACH, C. 1992 A continuum method for modeling surface tension. *J. Comput. Phys.* **100**, 335–354.

BURTON, J.C. & TABOREK, P. 2011 Simulations of Coulombic fission of charged inviscid drops. *Phys. Rev. Lett.* **106** (14), 144501.

CLOUPEAU, M. & PRUNET-FOCH, B. 1989 Electrostatic spraying of liquids in cone-jet mode. *J. Electrostat.* **22**, 135–159.

COFFMAN, C., MARTÍNEZ-SÁNCHEZ, M., HIGUERA, F.J. & LOZANO, P.C. 2016 Structure of the menisci of leaky dielectric liquids during electrically-assisted evaporation of ions. *Appl. Phys. Lett.* **109** (23), 231602.

COFFMAN, C.S., MARTÍNEZ-SÁNCHEZ, M. & LOZANO, P.C. 2019 Electrohydrodynamics of an ionic liquid meniscus during evaporation of ions in a regime of high electric field. *Phys. Rev.* E **99** (6), 063108.

COLLINS, R.T., JONES, J.J., HARRIS, M.T. & BASARAN, O.A. 2008 Electrohydrodynamic tip streaming and emission of charged drops from liquid cones. *Nat. Phys.* **4** (2), 149–154.

COLLINS, R.T., SAMBATH, K., HARRIS, M.T. & BASARAN, O.A. 2013 Universal scaling laws for the disintegration of electrified drops. *Proc. Natl Acad. Sci.* **110** (13), 4905–4910.

COMSOL, INC. 2019 *Comsol Multiphysics Reference Manual*. COMSOL.

COURANT, R., FRIEDRICHS, K. & LEWY, H. 1967 On the partial difference equations of mathematical physics. *IBM J. Res. Dev.* **11**, 215–234.

DE JUAN, L. & FERNÁNDEZ DE LA MORA, J. 1997 Charge and size distributions of electrospray drops. *J. Colloid Interface Sci.* **186** (2), 280–293.

DING, H., GILANI, M.N. & SPELT, P.D. 2010 Sliding, pinch-off and detachment of a droplet on a wall in shear flow. *J. Fluid Mech.* **664**, 217–244.

DOYLE, A., MOFFETT, D.R. & VONNEGUT, B. 1964 Behavior of evaporating electrically charged droplets. *J. Colloid Sci.* **19** (2), 136–143.

DUFT, D., ACHTZEHN, T., MÜLLER, R., HUBER, B.A. & LEISNER, T. 2003 Rayleigh jets from levitated microdroplets. *Nature* **421** (6919), 128.

FERNÁNDEZ DE LA MORA, J. & LOSCERTALES, I.G. 1994 The current emitted by highly conducting Taylor cones. *J. Fluid Mech.* **260**, 155–184.

FONTELOS, M.A., KINDELÁN, U. & VANTZOS, O. 2008 Evolution of neutral and charged droplets in an electric field. *Phys. Fluids* **20**, 092110.

GAÑÁN-CALVO, A.M., LÓPEZ-HERRERA, J.M., HERRADA, M.A., RAMOS, A. & MONTANERO, J.M. 2018 Review on the physics of electrospray: from electrokinetics to the operating conditions of single and coaxial Taylor cone-jets, and ac electrospray. *J. Aerosol Sci.* **125**, 32–56.

GALLUD, X. & LOZANO, P.C. 2022 The emission properties, structure and stability of ionic liquid menisci undergoing electrically assisted ion evaporation. *J. Fluid Mech.* **933**, A43.

GAMERO-CASTAÑO, M. & FERNÁNDEZ DE LA MORA, J. 2000 Direct measurement of ion evaporation kinetics from electrified liquid surfaces. *J. Chem. Phys.* **113** (2), 815–832.

GAMERO-CASTAÑO, M. & FERNÁNDEZ DE LA MORA, J. 2000*a* Direct measurement of ion evaporation kinetics from electrified liquid surfaces. *J. Chem. Phys.* **113** (2), 815–832.

GAMERO-CASTAÑO, M. & FERNÁNDEZ DE LA MORA, J. 2000*b* Kinetics of small ion evaporation from the charge and mass distribution of multiply charged clusters in electrosprays. *J. Mass Spectrom.* **35** (7), 790–803.

GAMERO-CASTAÑO, M. & FERNÁNDEZ DE LA MORA, J. 2000*c* Mechanisms of electrospray ionization of singly and multiply charged salt clusters. *Anal. Chim. Acta* **406** (1), 67–91.

GAMERO-CASTAÑO, M. & MAGNANI, M. 2019 Numerical simulation of electrospraying in the cone-jet mode. *J. Fluid Mech.* **859**, 247–267.

GAMERO-CASTAÑO, M. & CISQUELLA-SERRA, A. 2020 Electrosprays of highly conducting liquids: a study of droplet and ion emission based on retarding potential and time-of-flight spectrometry. *Phys. Rev. Fluids* **6** (1), 013701.

GAÑÁN-CALVO, A.M., LÓPEZ-HERRERA, J.M., REBOLLO-MUNOZ, N. & MONTANERO, J.M. 2016 The onset of electrospray: the universal scaling laws of the first ejection. *Sci. Rep.* **6** (1), 1–9.

GARZON, M., GRAY, L.J. & SETHIAN, J.A. 2014 Numerical simulations of electrostatically driven jets from nonviscous droplets. *Phys. Rev.* E **89** (3), 033011.

GAWANDE, N., MAYYA, Y.S. & THAOKAR, R. 2017 Numerical study of rayleigh fission of a charged viscous liquid drop. *Phys. Rev. Fluids* **2** (11), 113603.

GAWANDE, N., MAYYA, Y.S. & THAOKAR, R. 2020 Jet and progeny formation in the rayleigh breakup of a charged viscous drop. *J. Fluid Mech.* **884**, A31.

GIGLIO, E., GERVAIS, B., RANGAMA, J., MANIL, B., HUBER, B.A., DUFT, D., MÜLLER, R., LEISNER, T. & GUET, C. 2008 Shape deformations of surface-charged microdroplets. *Phys. Rev.* E **77** (3), 036319.

GIGLIO, E., RANGAMA, J., GUILLOUS, S. & LE CORNU, T. 2020 Influence of the viscosity and charge mobility on the shape deformation of critically charged droplets. *Phys. Rev.* E **101** (1), 013105.

GOMEZ, A. & TANG, K. 1994 Charge and fission of droplets in electrostatic sprays. *Phys. Fluids* **6** (1), 404–414.

HERRADA, M.A., LÓPEZ-HERRERA, J.M., GAÑÁN-CALVO, A.M., VEGA, E.J., MONTANERO, J.M. & POPINET, S. 2012 Numerical simulation of electrospray in the cone-jet mode. *Phys. Rev.* E **86**, 026305.

HIGUERA, F.J. 2008 Model of the meniscus of an ionic-liquid ion source. *Phys. Rev.* E **77** (2), 026308.

HOGAN, C.J. JR. & FERNÁNDEZ DE LA MORA, J. 2009 Tandem ion mobility-mass spectrometry (IMS-MS) study of ion evaporation from ionic liquid-acetonitrile nanodrops. *Phys. Chem. Chem. Phys.* **11** (36), 8079–8090.

HUH, H. & WIRZ, R.E. 2022 Electrohydrodynamic simulation of electrospray thruster extraction. *AIAA Paper* 2022-1359.

IRIBARNE, J.V. & THOMSON, B.A. 1976 On the evaporation of small ions from charged droplets. *J. Chem. Phys.* **64** (6), 2287–2294.

JACQMIN, D. 1999 Calculation of two-phase Navier–Stokes flows using phase-field modelling. *J. Comput. Phys.* **155**, 96–127.

JACQMIN, D. 2000 Contact-line dynamics of a diffuse fluid interface. *J. Fluid Mech.* **402**, 57–88.

KATTA, V., ROCKWOOD, A.L. & VESTAL, M.L. 1991 Field limit for ion evaporation from charged thermospray droplets. *Intl J. Mass Spectrom.* **103** (2–3), 129–148.

LABOWSKY, M. 1998 Discrete charge distributions in dielectric droplets. *J. Colloid Interface Sci.* **206** (1), 19–28.

LABOWSKY, M., FENN, J.B. & FERNÁNDEZ DE LA MORA, J. 2000 A continuum model for ion evaporation from a drop: effect of curvature and charge on ion solvation energy. *Anal. Chim. Acta* **406** (1), 105–118.

LOSCERTALES, I.G. & FERNÁNDEZ DE LA MORA, J. 1995 Experiments on the kinetics of field evaporation of small ions from droplets. *J. Chem. Phys.* **103** (12), 5041–5060.

LUEDTKE, W.D., LANDMAN, U., CHIU, Y.H., LEVANDIER, D.J., DRESSLER, R.A., SOK, S. & GORDON, M.S. 2008 Nanojets, electrospray, and ion field evaporation: molecular dynamics simulations and laboratory experiments. *J. Phys. Chem.* A **112** (40), 9628–9649.

LÓPEZ-HERRERA, J.M., GAÑÁN-CALVO, A.M., POPINET, S. & HERRADA, M.A. 2015 Electrokinetic effects in the breakup of electrified jets: a volume-of-fluid numerical study. *Intl J. Multiphase Flow* **71**, 14–22.

LÓPEZ-HERRERA, J.M., POPINET, S. & HERRADA, M.A. 2011 A charge-conservative approach for simulating electrohydrodynamic two-phase flows using volume-of-fluid. *J. Comput. Phys.* **230**, 1939–1955.

MANDAL, S., GHOSH, U., BANDOPADHYAY, A. & CHAKRABORTY, S. 2015 Electro-osmosis of superimposed fluids in the presence of modulated charged surfaces in narrow confinements. *J. Fluid Mech.* **776**, 390–429.

MELCHER, J.R. & TAYLOR, G.I. 1969 Electrohydrodynamics: a review of the role of interfacial shear stresses. *Annu. Rev. Fluid Mech.* **1**, 111–146.

MILLER, S.W., ULIBARRI-SANCHEZ, J.R., PRINCE, B.D. & BEMISH, R.J. 2021 Capillary ionic liquid electrospray: beam compositional analysis by orthogonal time-of-flight mass spectrometry. *J. Fluid Mech.* **928**, A12.

MISRA, K. 2020 Magnetic (electric) drop deformation in uniform external fields: volume averaged methods and formation of static and dynamic conical tips. *Phys. Fluids* **32** (10), 107104.

MISRA, K. & GAMERO-CASTAÑO, M. 2022 Leaky-dielectric phase field model for the axisymmetric breakup of an electrified jet. *Phys. Rev. Fluids* **7** (6), 064004.

PEREZ-LORENZO, L.J. & FERNÁNDEZ DE LA MORA, J. 2022 Probing electrically driven nanojets by energy and mass analysis in vacuo. *J. Fluid Mech.* **931**, A4.

PILLAI, R., BERRY, J.D., HARVIE, D.J. & DAVIDSON, M.R. 2016 Electrokinetics of isolated electrified drops. *Soft Matt.* **12** (14), 3310–3325.

RADCLIFFE, A.J. 2013 Non-conforming finite elements for axisymmetric charged droplet deformation dynamics and coulomb explosions. *Intl J. Numer. Meth. Fluids* **71** (2), 249–268.

RAYLEIGH, LORD 1882 On the equilibrium of liquid conducting masses charged with electricity. *Phil. Mag.* **14** (87), 184–186.

RICHARDSON, C.B., PIGG, A.L. & HIGHTOWER, R.L. 1989 On the stability limit of charged droplets. *Proc. Math. Phys. Engng Sci.* **422** (863), 319–328.

ROGHAIR, I., MUSTERD, M., ENDE, D., KLEIJN, C., KRUETZER, M. & MUGELE, F. 2015 A numerical technique to simulate display pixels based on electrowetting. *Microfluid. Nanofluid.* **19**, 465–482.

ROSELL-LLOMPART, J., GRIFOLL, J. & LOSCERTALES, I.G. 2018 Electrosprays in the cone-jet mode: from Taylor cone formation to spray development. *J. Aerosol Sci.* **125**, 2–31.

ROULLEAU, M. & DESBOIS, M. 1972 Study of evaporation and instability of charged water droplets. *J. Atmos. Sci.* **29**, 565–569.

SAVILLE, D. 1997 Electrohydrodynamics: the Taylor–Melcher leaky dielectric model. *Annu. Rev. Fluid Mech.* **29** (1), 27–64.

SCHWEIZER, J.W. & HANSON, D.N. 1971 Stability limit of charged drops. *J. Colloid Interface Sci.* **35** (3), 417–423.

TAFLIN, D.C., WARD, T.L. & DAVIS, E.J. 1989 Electrified droplet fission and the rayleigh limit. *Langmuir* **5** (2), 376–384.

TAYLOR, G.I. 1964 Disintegration of water drops in an electric field. *Proc. R. Soc.* A **280** (1382), 383–397.

THOMSON, B.A. & IRIBARNE, J.V. 1979 Field induced ion evaporation from liquid surfaces at atmospheric pressure. *J. Chem. Phys.* **71** (11), 4451–4463.

TOMAR, G., GERLACH, D., BISWAS, G., ALLEBORN, N., SHARMA, A., DURST, F., WELCH, S.W.J. & DELGADO, A. 2007 Two-phase electrohydrodynamic simulations using a volume-of-fluid approach. *J. Comput. Phys.* **227** (2), 1267–1285.

WANG, Q., MA, M. & SIEGEL, M. 2019 Deformation and stability of a viscous electrolyte drop in a uniform electric field. *Phys. Rev. Fluids* **4** (5), 053702.

YUE, P., FENG, J.J., LIU, C. & SHEN, J. 2004 A diffuse-interface method for simulating two-phase flows of complex fluids. *J. Fluid Mech.* **515**, 293–317.

ZELENY, J. 1917 Instability of electrified liquid surfaces. *Phys. Rev.* **10**, 1–16.